# Mass transfer to reactive boundaries from steady three-dimensional flows in microchannels

Joseph D. Kirtland
*Department of Physics, Cornell University, Ithaca, New York 14853*

Gregory J. McGraw[a] and Abraham D. Stroock[b]
*School of Chemical and Biomolecular Engineering, Cornell University, Ithaca, New York 14853*

(Received 13 January 2006; accepted 21 June 2006; published online 25 July 2006)

This paper presents a numerical study of the effect of transverse secondary flows on mass transfer to reactive boundaries in microchannels. The geometry considered is relevant to surface catalyzed reactions, fuel cells, biochemical sensors, and other microreactor applications. The 3D flows that we consider approximate flows that are experimentally achievable through topographical patterning of one wall of a microchannel, as in the Staggered Herringbone Mixer (SHM) and similar geometries. We simulate a mass transfer process using passive tracers to model reactive solute molecules in a Stokes flow (Reynolds number, $\mathrm{Re}=0$) over a range of Péclet number, $10^2 \leqslant \mathrm{Pe} \leqslant 10^5$, with instantaneous kinetics at the reactive boundary. Our simulation allows for the evaluation of the local Sherwood number produced by a uniaxial Poiseuille flow and several chaotic and nonchaotic 3D flows. In chaotic flows, the local Sherwood number evolves in a simple manner that shares features with the classic Graetz solution for transfer from a uniaxial pipe flow: an entrance region with cube-root scaling in the Graetz number and a constant asymptotic value. This "Modified Graetz" behavior also differs in important ways from the standard case: the entrance length is Pe independent and the asymptotic rate of transfer is Pe dependent and potentially much greater than in the uniaxial case. We develop a theoretical model of the transfer process; the predictions of this model compare well with simulation results. We use our results to develop a correlation for the mass transfer in laminar channel flows, to elucidate the importance of chaos in defining transfer in these flows, and to provide design rules for microreactors with a single reactive wall. © *2006 American Institute of Physics*. [DOI: 10.1063/1.2222389]

## I. INTRODUCTION

Mass transfer to reactive boundaries is of great technological relevance in fields ranging from industrial chemical engineering to analytical biochemistry. Surface catalyzed reactions,[1] electrochemical reactions as in fuel cells,[2–4] and surface interactions as in biological sensors[5–7] all rely on the delivery of solute to solid boundaries. The more efficient this delivery is, the higher the yield (e.g., in surface catalyzed reactions), fuel efficiency and current density (e.g., in fuel cells), or speed of analysis (e.g., in sensors) will be. Significant efforts are being made to translate these processes to microfluidic platforms in order to allow for portability, to decrease sample volumes, and to increase rates of operation. In standard microchannels, rectangular ducts with constant cross-sectional dimensions of $10-10^3$ $\mu$m and an axial dimension of $10^{-1}-10^2$ cm, achieving efficient mass transfer can pose a particular challenge. In a rectangular microchannel, pressure-driven flows are uniaxial with low Reynolds number, $\mathrm{Re}=UH/\nu<100$, and high Péclet number, $\mathrm{Pe}=UH/D>100$, where $U$ (m/s) is the average axial velocity, $H$ (m) is the characteristic dimension of the channel, $\nu$ ($\mathrm{m}^2/\mathrm{s}$) is the kinematic viscosity of the fluid, and $D$ ($\mathrm{m}^2/\mathrm{s}$) is the diffusivity of the solute in the fluid; mass transfer toward reactive boundaries is purely diffusive and slow relative to convection. In this low Re, high Pe regime, there is an inevitable compromise between high flux (e.g., with fast flows) and efficient use of reagents (e.g., with slow flows that allow reagents to diffuse to the surface). Many researchers have shown that three-dimensional (3D) flows created with laminar mixers can moderate this compromise by increasing rates of transfer relative to uniaxial laminar flow.[8,9] Nonetheless, we are unaware of a predictive model of this effect that is appropriate for the design of microreactors or laminar reactors more generally.

In this article, we present numerical and theoretical studies that elucidate the effect of steady, three-dimensional flows on rates of mass transfer to boundaries in microchannels. We develop and validate predictive correlations for rates of transfer, address the outstanding question of the mechanism by which Langrangian chaos influences transfer to boundaries, and translate our findings into specific design rules for microfluidic reactors. We employ an approximate model of the 3D flows that can be achieved with the incorporation of obliquely oriented grooves in one wall of a microchannel, as in the Staggered Herringbone Mixer (SHM).[10] Figure 1 presents a schematic diagram of the SHM and the geometry used here to approximate the flow in the SHM.

[a]Present address: Applied Physics Program, University of Michigan, Ann Arbor, Michigan 48109-1120.
[b]Author to whom correspondence should be addressed. Electronic mail: ads10@cornell.edu

 

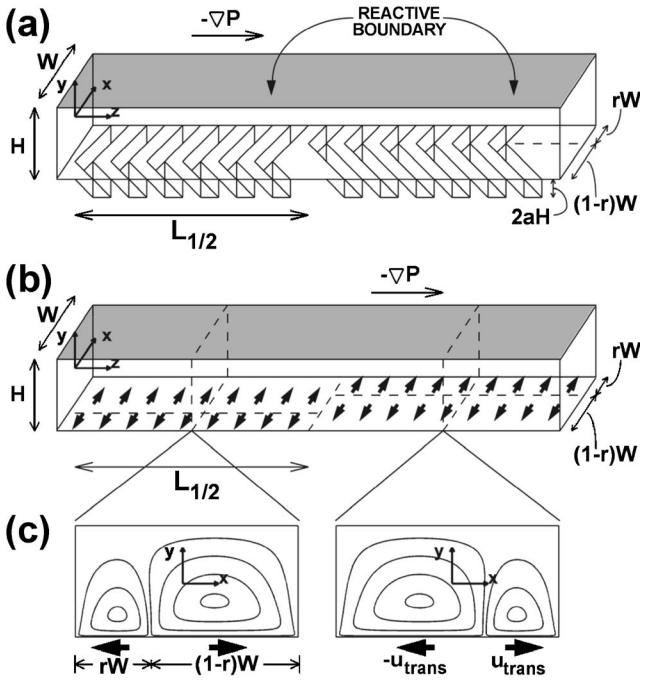


FIG. 1. Schematic diagram of the staggered herringbone mixer (SHM) and of the lid-driven cavity model of the flow in such a structure. (a) One cycle of the SHM. Grooves along the floor induce transverse secondary flows when a steady pressure gradient is applied along the channel. (b) Lid-driven cavity approximation of the SHM. Transversely (along $x$) slipping regions on a smooth boundary generate transverse flows that mimic those induced by grooves. (c) Streamlines of cross-sectional flow produced by lid-driven cavity approximation of the SHM. The degree of asymmetry $r$ and the half-cycle length $L_{1/2}$ can be tailored to produce regular or chaotic flow (Ref. 12).

Figure 1(a) shows one cycle of a typical SHM device. These structures can be fabricated by standard lithographic techniques. Our model flow mimics the effect of the grooves by replacing the grooved surface with a flat boundary with transverse slip velocities, as indicated in Fig. 1(b).[11,12] The streamlines of the transverse flow field generated by these slip velocities are presented in Fig. 1(c).

We simulate convection-diffusion-reaction in this model flow to calculate the rate of mass transfer to a single reactive boundary on the wall opposite the grooved surface that induces the transverse flow. We focus on transfer to this unstructured boundary for several reasons: it is representative of a generic no-slip boundary in a three-dimensional duct flow; our model, while accurate in the bulk and near the far wall, does not capture the true geometrical detail near the patterned surface; and this reactor geometry involving a flat reactive wall opposite a topographically patterned wall is experimentally convenient because a microchannel with mixing grooves can simply be sealed against a flat reactive surface. Our model assumes a Stokes flow ($\mathrm{Re}=0$); we take this limit to simulate flows with low to moderate Re ($\mathrm{Re}<10$). We consider Péclet numbers in the range, $10^2 \leqslant \mathrm{Pe} \leqslant 10^5$. Our model assumes instantaneous kinetics at the reactive boundary. For systems with finite chemical rate constants at the boundaries, the conclusions presented here are still instructive; in those cases, mass transfer resistances predicted here would need to be added in series with those due to the finite surface rate constant to find the overall resistance to transfer.[13]

Transfer to solid boundaries from 3D laminar flows has been studied in a variety of systems.[1,14–23] Heat transfer has been studied in more detail than mass transfer in these systems; this work tends to consider a low Pe regime due to the high diffusivity of heat, but it is otherwise analogous to questions of mass transfer. Chang and Sen have identified two distinct classes of transfer:[8] transfer of solute from one boundary to another across the flow[14,16–19] and transfer of solute between the bulk and the wall (i.e., to fill or empty the solute from the bulk);[1,15,20–23] our study falls into the category of bulk-to-wall transfer. Studies have also considered transfer to slip[14–19] and no-slip[1,20–23] boundaries; our choice of reactor geometry simulates a no-slip reactive boundary. Analysis of rates of transfer have been performed in the entrance region (small axial distance) and in the asymptotic region (large axial distance), and results have been quoted for various quantities such as the flux, transfer coefficient, efficiency, or effective diffusivity. We present correlations for the Sherwood number, Sh, a nondimensionalized mass transfer coefficient (see Sec. III for definition). We analyze both the entrance and asymptotic regions. The most useful studies for comparison to our results are those involving heat transfer in coiled tubes[20–22] and mass transfer in static mixers.[1] Janssen *et al.*, and Acharya *et al.*, found results similar to our own for scaling at small axial distance, but different scaling at large distances.[20,22] Mokrani *et al.*, cite an increase in the rates of transfer due to chaotic flow relative to nonchaotic flow, but do not investigate the origin of this effect.[21] These studies will be further discussed with respect to our own results in Sec. IV B. A clear understanding of the mechanism of mass transfer in 3D laminar flows has yet to be presented; we probe that mechanism in the work presented here.

The remainder of this paper is organized as follows: in Sec. II, we outline the geometry of our system and describe the model of the flow and the simulation of convection-diffusion-reaction within this flow. In Sec. III, we supply theoretical background on mass transfer and outline the Lévêque solution as it relates to our analysis, identifying correlations for quantities relevant to mass transfer. In Sec. IV A, we present results from our simulations for mass transfer in various flows. In Sec. IV B, we interpret the results in terms of the Lévêque analysis and the correlations presented in Sec. III, and discuss our results for the rates of mass transfer due to transverse flows in relation to results in the literature. At the end of Sec. IV B, we summarize the features of flows that are important for increasing transfer to boundaries and explain how such flows can affect the design of efficient microreactors.

## II. MODEL AND SIMULATION DETAILS

We performed simulations of convection-diffusion-reaction by tracking the advection of passive tracers in a flow field down the length of a microchannel. This flow field is the solution of the equations of motion for a physical situation that approximates the flow in the actual staggered herringbone structure (see Fig. 1). Domain perturbation analysis

suggests that a simple transverse slip velocity along a smooth wall can be used to replace the mean effect of the obliquely oriented grooves.[11] Taking this suggestion literally, our model flow corresponds to that of a three-dimensional lid-driven cavity with axial pressure-driven flow. A complete description of this model is given elsewhere.[12] Figure 1(a) shows the physical structure of an experimental device. Figure 1(b) shows the lid-driven cavity approximation of the actual structure. Figure 1(c) shows the streamlines of the cross-sectional flow produced in the lid-driven cavity approximation. The parameters that control the character of the model flow are the degree of asymmetry of the pattern of slip on the bottom boundary, $r$, the length of a half cycle, $L_{1/2}$, the aspect ratio of the channel cross section, $\omega = W/H$, and the magnitude of the slip velocity, $u_{\text{trans}}$. The slip velocity can be related to the structure of the grooves in the actual SHM, as described elsewhere.[11] We take the axial velocity to be the Poiseuille flow in a duct:

$$u_z(x,y) = 1 - y^2 + 4\sum_{n=1}^{\infty} \frac{(-1)^n}{\gamma_n^3 \cosh(\gamma_n \omega)} \cosh(\gamma_n x)\cos(\gamma_n y), \tag{1}$$

where $\gamma_n = (2n-1)\pi/2$. While physical grooves would perturb the axial flow in addition to creating a transverse flow, we neglect this higher order perturbation and preserve the simple Poiseuille flow.

The effective transverse slip along the floor causes the flow to recirculate in the cross section, producing two counter rotating eddies or vortices for herringbone-shaped grooves, as in Fig. 1(c). The relative size of the eddies is determined by the degree of asymmetry, $r$. At the end of each half cycle, the flow is inverted in the cross-stream direction (along $x$), such that the larger and smaller eddies switch sides. This periodic switching leads to an interesting aspect of the flow; as can be seen in Fig. 1(c) the streamlines of the flow in the cross section in one half-cycle cross those of the other half-cycle; this change in the structure of the flow causes the trajectories of particles that were following similar paths to diverge from one another. In the continuum sense, a region of the cross section that had been a part of one vortex is suddenly part of the other vortex. The presence of these eddies and the crossing of the streamlines as the flow alternates provide the stretching and folding, respectively, which are required for Lagrangian chaos.[24] For symmetrical flows (e.g., $r=1$ or $r=1/2$), the form of the transverse flow does not vary with the axial position, and the flows are 3D, but nonchaotic.

We used the solution for the two-dimensional flow in a lid-driven cavity as presented in detail in Appendix A of Ref. 12. Briefly, in the Stokes regime, the momentum balance can be expressed as the biharmonic equation for the stream function in the cross section. We used a double Fourier series in $x$ and $y$ to approximate the solution to this equation and satisfy the slip and no-slip boundary conditions. In our simulation, we took this solution for the transverse flow and we used Eq. (1) for the axial flow. We used 10 Fourier terms in the calculation of the axial flow and 20 Fourier terms total (10 in the $x$ direction and 10 in the $y$ direction) in the calculation of the transverse flow. We chose to evaluate and tabulate the velocity field at a large number of grid points in the cross section. We then interpolated from this table at a given $(x,y)$ to find the velocity during the particle tracking. We used a lookup table of $1024 \times 512$ grid points and a third order interpolation scheme in each direction for each of the velocity components.[25]

In cases that involved varying the transverse flow along $z$, we switched the velocity instantaneously at the end of each half-cycle. This approximate treatment of the transition with a discontinuity is reasonable for flows at low Re for which the transition region will be short. We have shown previously that this model produces results that are consistent with experiment in studies of mixing in the bulk.[12]

We seeded particles into the flow at $z=0$ with the probability of a given initial position $(x,y)$ at $z=0$ taken to be proportional to the axial velocity at that point. This seeding strategy approximates the flux of the solute through the plane at $z=0$ for a solution of uniform initial concentration. We imposed these initial conditions by the rejection method.[25] We updated the position of the particle by integration of the velocity field using a fifth order Runge-Kutta method. This method is more accurate than the standard fourth order Runge-Kutta method, and it also furnishes an estimate of the numerical error associated with the operation. Using this estimate of the error, an adaptive step size algorithm allowed the particle to take large steps through regions where the gradients of velocity were small, and required smaller steps through regions where the gradients were large.[25] This integration method improved both the efficiency through the simpler regions of the flow and the accuracy through the more complicated regions of the flow relative to nonadaptive methods.

A diffusive step was implemented during each convective time step. We took this diffusive step as a separable random walk in $x$, $y$, and $z$ with the step size chosen as a Gaussian random number with a mean of zero and a standard deviation of the form $\Delta x = \sqrt{2D\Delta t}$, where $D$ is the diffusivity of the particle and $\Delta t$ is the time step used in the corresponding convective step. This results in a three-dimensional, isotropic, diffusive displacement, which is appropriate for modeling diffusion over finite time steps.[26] The time step was constrained such that at $\text{Pe} = 10^2$, 85% of the diffusive steps were less than 1% of the channel height, and 99.5% were less than 2% of the channel height. At higher values of Pe, similar time steps produce smaller diffusive displacements, and therefore the above values are an upper bound on the distributions of diffusive displacements for all of the cases studied here. If at any time the particle left the channel, it reflected specularly across the wall that it crossed back into the flow. We noted the $x,z$ position of the first crossing of a reactive wall for each particle and considered this to be the position at which it reacted. This strategy allowed for calculation of reactive flux. We also noted the position $(x,y)$ in the cross section as each particle crossed regularly spaced axial positions; we used this information to calculate concentration profiles as a function of axial distance. We evaluated the axial convective flux by binning the particles in evenly spaced bins in the cross section at each axial position of

interest. We then determined the concentration in each bin by dividing by the average axial velocity in that bin. The total number of particles was approximately 200 000 in simulations of uniaxial flow and the chaotic flow shown in Figs. 1(b) and 1(c) ($r=1/3$, $L_{1/2}=10H$), and approximately 50 000 in all other simulations; the smaller number of particles proved sufficient to ensure convergence of the calculated profile of concentration and flux.

We tested the overall accuracy of the interpolation and integration schemes by tracking particles in a single vortex flow ($r=1$) with a periodic switch in the overall sign of the slip velocity at the floor. In this flow, the cross-sectional position of a particle at the end of each full cycle should be invariant. The drift introduced by velocity interpolation and finite step size integration was roughly linear in time and very small. Over the maximum axial length considered (2000 $H$), this drift was four orders of magnitude smaller than the displacement that would arise due to physical diffusion at $\mathrm{Pe}=10^6$. For smaller Pe, the effect of physical diffusion is greater, such that the relative importance of the drift is smaller. We concluded that the accuracy of the interpolation and integration method was sufficient for all Pe considered in this work.

As a measure of the Lagrangian character of the flows considered, we created Poincaré sections for several initial conditions by recording the position in the cross section at the end of each cycle ($z=0$, 2 $L_{1/2}$, 4 $L_{1/2}$, …, where $L_{1/2}$ is the half-cycle length as in Fig. 1), with a diffusivity of zero ($\mathrm{Pe}=0$). Figure 2 presents these Poincaré sections and shows the distinctions between the various flows considered. Figure 2(a) demonstrates the chaotic advection associated with a staggered herringbone design ($r=1/3$; $L_{1/2}=10H$) that we know gives good mixing in the bulk of the flow.[10,12] Two of the initial conditions belonged to a chaotic invariant set that spans much of the cross section. The third initial condition remained confined to a nonchaotic island in the upper right corner. Figures 2(b) and 2(c) show the periodic orbits associated with nonchaotic flows that do not change in the axial direction due to their symmetry under reflection across the $y$ axis ($r=1/2$ and $r=1$). Figure 2(d) presents the Poincaré map of a flow with the same asymmetry as in Fig. 2(a) ($r=1/3$) but with a cycle length that was one quarter of the cycle length in Fig. 2(a), $L_{1/2}=2.5H$.[27] This situation led to a less chaotic flow: while the invariant set for the first initial condition spanned a large fraction of the cross section, the second initial condition was quasiperiodic near the core of the right vortex. The third initial condition was still confined in the island in the upper right corner. We note that these Poincaré maps indicate dramatic differences in the Lagrangian character of these flows *in the bulk*. We will see in Sec. IV that the differences in rates of mass transfer to boundaries in these different flows are more subtle than the effects in the bulk.

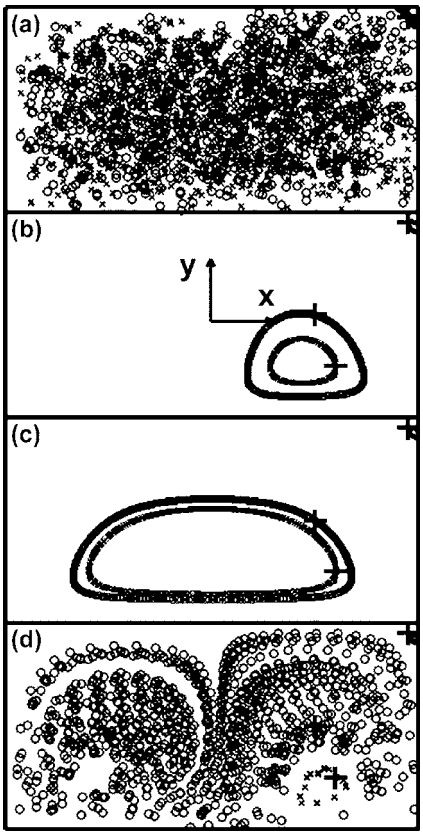


FIG. 2. Poincaré sections for several flow geometries: (a) $r=\frac{1}{3}$, $L_{1/2}=10H$; (b) $r=\frac{1}{2}$; (c) $r=1$; (d) $r=\frac{1}{3}$, $L_{1/2}=2.5H$. For all cases, the ratio of transverse velocity to axial velocity $u_{\mathrm{trans}}/U=0.2$. Three initial conditions $(x,y)=(1,0)$ (circles), $(1.2,-0.5)$ (crosses), and (1.9, 0.9) (points, trapped in upper right corner) are tracked through a length equivalent to 20 000 channel heights, where $(x,y)=(0,0)$ is the center of the cross section. Large crosses mark the three initial positions, most easily seen in frames (b) and (c).

## III. THEORY

### A. Mass transfer background

We represent the rate of mass transfer to boundaries with the local Sherwood number, $\mathrm{Sh}(z)$, a dimensionless measure of the local mass transfer coefficient averaged over the width of the channel (along $x$). In various contexts, Sh is an indicator of efficiency of reagent use, current density, or sensor response time.[28] The local Sherwood number is defined as

$$\mathrm{Sh}(z)=\frac{k(z)H}{D}, \tag{2}$$

where $k(z)$ (m/s) is the local mass transfer coefficient averaged over the width of the channel (along $x$), $H$ (m) is the height of the channel, and $D$ ($\mathrm{m}^2/\mathrm{s}$) is the diffusivity of the reactive species. The average local coefficient of mass transfer is further defined as

$$k(z)=-\frac{J(z)}{C_b(z)-C_s(z)}, \tag{3}$$

where $J(z)$ ($\mathrm{mol/m^2s}$) is the local reactive flux averaged across the width of the reactive boundary (along $x$), $\mathrm{C}_b(z)$ ($\mathrm{mol/m^3}$) is the average bulk concentration, and $C_s(z)$ ($\mathrm{mol/m^3}$) is the average concentration at the surface. For a system with fast kinetics, the concentration at the reactive surface, $\mathrm{C}_s(z)\to 0$. We take the average bulk concentration as the cup-mixing concentration $C_{\mathrm{cup}}(z)$ ($\mathrm{mol/m^3}$):[13]

$$C_{\text{cup}}(z) = \frac{\int\int C(x,y,z)u_z(x,y)dxdy}{\int\int u_z(x,y)dxdy} = \frac{\int\int C(x,y,z)u_z(x,y)dxdy}{UA}, \tag{4}$$

where $u_z(x,y)$ (m/s) is the axial velocity as a function of position $(x,y)$ in the cross section, $U$ (m/s) is the average axial velocity, $A$ ($m^2$) is the cross-sectional area, and the integrals are taken over the cross section of the channel. It can be shown by conservation of mass that the reactive flux $J(z)$ is

$$J(z) = UH\frac{dC_{\text{cup}}}{dz}. \tag{5}$$

Combining Eqs. (2), (3), and (5) gives the following form for Sh:

$$\text{Sh}(z) = -\frac{\text{Pe}H}{C_{\text{cup}}(z)}\frac{dC_{\text{cup}}}{dz} = -\frac{d\ln C_{\text{cup}}}{d\frac{z}{\text{Pe}H}}. \tag{6}$$

The Sherwood number can therefore be viewed as a relative rate of change in $C_{\text{cup}}$ with respect to the nondimensional axial distance traveled along the reactive boundary. This dimensionless distance is the inverse of the Graetz number, $\text{Gz}=\text{Pe}H/z$.

As we will see in Sec. IV even in the presence of complex transverse flows, the mass transfer phenomenon we consider here shares important characteristics with the classic Graetz problem for heat transfer to the boundary of a uniaxial pipe flow.[13] We recall here the key aspects of that result: a concentration boundary layer appears at the leading edge of the reactive surface and grows in the direction normal to the reactive surface (along $y$, Fig. 1) with increasing axial distance from the leading edge. This growth is due to the depletion of solute from the region adjacent to the reactive surface, and continues until this concentration boundary layer fills the height of the channel. Beyond this point, the concentration distribution decays in a self-similar manner. This transition to self-similarity defines the end of the entrance region, and, from this point on, $\text{Sh}(z)$ becomes constant; we refer to this region of constant Sh as the asymptotic or plateau region. In uniaxial flows, the plateau value, $\text{Sh}_{\text{plat}}$, is geometry-dependent and Pe-independent and has been calculated for flow in a round pipe ($\text{Sh}_{\text{plat}}=3.657$) and between two reactive plates ($\text{Sh}_{\text{plat}}=7.541$);[13] geometries with less symmetry (e.g., a single reactive wall in a rectangular duct) are more difficult to analyze analytically. It will suffice to say that the end of the entrance region, $z=z_{\text{plat}}$, occurs when the boundary layer is roughly the size of the channel, and Sh is of order 1. In these cases, the length of the entrance region scales as, $z_{\text{plat}}\sim\text{Pe}\,H$, or, in other words, it corresponds to a constant value of the Graetz number, $\text{Gz}_{\text{plat}}=\text{Pe}\,H/z_{\text{plat}}$.

### B. Mass transfer from a simple shear flow

To build a basis with which to model mass transfer in three-dimensional flows, we consider the transfer of mass to the surface of an infinite plate in a fully developed shear flow as shown in Fig. 3(a); this is the classic Lévêque problem. The plate is analogous to the reactive wall of a duct in the vicinity of the wall where the Poiseuille flow can be approximated by a simple shear flow and the shear rate at the wall is related to the average bulk velocity and the height of the duct. The plate lies in the plane $y=0$ and is reactive for $z>0$. Assuming that the flow is a simple shear flow and that streamwise diffusion is negligible compared to convection ($\text{Pe}\gg 1$), the steady-state convective diffusion equation to be solved is

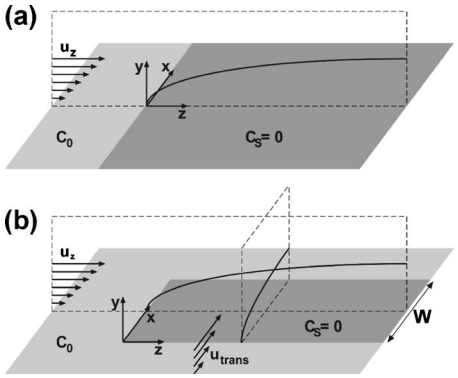


FIG. 3. Developing boundary layers over a reactive plate. (a) Development of a boundary layer in a uniaxial flow. (b) Simplified model of the simultaneous growth of axial and transverse concentration boundary layers over an isolated reactive boundary. The transverse boundary layer can truncate the growth of the axial boundary layer.

$$\mathbf{u}\cdot\nabla C = D\nabla^2 C \rightarrow u_z(y)\frac{\partial C}{\partial z} = D\frac{\partial^2 C}{\partial y^2}, \qquad u_z(y) = \dot{\gamma}y, \tag{7}$$

with boundary conditions

$$C(y,z\leqslant 0) = C_0, \qquad C(y=0,z>0) = 0, \qquad C(y\rightarrow\infty,z) = C_0, \tag{8}$$

where $\mathbf{u}=u_z(y)\hat{z}$ (m/s) is the velocity field, $\dot{\gamma}=\partial u_z/\partial y$ ($s^{-1}$) is the shear rate at the plate surface, and $C_0$ ($\text{mol}/\text{m}^3$) is the concentration far from the surface or, equivalently, the inlet concentration. The zero concentration boundary condition at the wall accounts for the reaction process for very fast reaction kinetics. A similarity solution gives the concentration profile:

$$C(\eta) = \frac{C_0}{\Gamma\left(\frac{4}{3}\right)}\int_0^{\eta} e^{-\lambda^3}d\lambda, \qquad \eta = \left(\frac{\dot{\gamma}}{9Dz}\right)^{1/3}y. \tag{9}$$

From this solution, the diffusive flux to the surface can be calculated:

$$J(z) = -D\left.\frac{\partial C}{\partial y}\right|_{y=0} = \frac{DC_0}{\Gamma\left(\frac{4}{3}\right)}\left(\frac{\dot{\gamma}}{9D}\right)^{1/3} z^{-1/3}, \tag{10}$$

which gives the following form for $\mathrm{Sh}(z)$:

$$\mathrm{Sh}(z) = \frac{1}{\Gamma\left(\frac{4}{3}\right)}\left(\frac{H^2\dot{\gamma}}{9D}\right)^{1/3}\left(\frac{z}{H}\right)^{-1/3}. \tag{11}$$

The assumption of a simple shear flow is not as constraining as it may seem. In the vicinity of a no-slip surface, flows can be approximated as a simple shear. For pressure-driven flow between parallel, smooth plates, the shear rate at the wall is

$$\dot{\gamma} = \left.\frac{\partial u_z}{\partial y}\right|_{y=0} = \frac{6U}{H}, \tag{12}$$

where $U$ is the average axial velocity, and $H$ is the plate separation. The shear rate at the wall for a general pressure-driven flow in a rectangular duct depends on the geometry of the duct. It is convenient to express the Sherwood number in terms of the ratio of shear rate at the reactive boundary to average axial velocity $U$ and the Péclet number Pe:

$$\mathrm{Sh}(z) = \frac{9^{-1/3}}{\Gamma\left(\frac{4}{3}\right)}\left(\frac{H\dot{\gamma}}{U}\right)^{1/3}\left(\frac{z}{\mathrm{Pe}\,H}\right)^{-1/3}, \tag{13}$$

where the dimensionless ratio $H\dot{\gamma}/U$ depends on the specific geometry of the channel and can be found by differentiating the axial velocity with respect to $y$ at the reactive wall. As a first approximation for the shear rate in a rectangular duct, we take the value, $\dot{\gamma}=6U/H$ for flow between parallel plates from Eq. (12) and use Eq. (13) to predict the following correlation for $\mathrm{Sh}(z)$ in a uniaxial duct flow:

$$\mathrm{Sh}(z) = B_0\left(\frac{z}{\mathrm{Pe}\,H}\right)^{-1/3}, \tag{14}$$

where $B_0$ is a geometry dependent constant that is $O(1)$ for the flows considered here.

### C. Mass transfer from a 3D duct flow and modified Graetz behavior

In this subsection, we extend the application of the Lévêque analysis to the transverse velocity components ($x$ and $y$ in Fig. 1) of a 3D flow through a duct. This approximate treatment was motivated by our observation of developing concentration boundary layers in the cross section of our simulated reactors, as presented in Sec. IV A. Chang and Sen mentioned the concept of transverse boundary layers,[8] and Xu *et al.* have observed these structures experimentally in a heat transfer study.[29] As we illustrate in the proceeding sections, this approach explains the key features of the observed phenomena and allows us to derive correlations for useful quantities.

We took the simple perspective depicted in Fig. 3(b) in order to model mass transfer from a 3D duct flow: we consider entirely distinct axial and transverse flows encountering the reactive surface. Conceptually, each of these flows will develop a concentration boundary layer via the Lévêque-type process as described in Sec. III B. A key feature of the transverse boundary layer is that its development is terminated once the fluid has traversed the width of the reactive surface, rather than growing indefinitely. If sufficiently strong, this transverse flow controls the development of the concentration distribution by convecting undepleted fluid to the edge of the reactive surface and thus arresting the growth of the axial boundary layer. By application of the standard Lévêque analysis for this transverse flow, it is possible to use Eq. (13) in the cross-stream direction (along $x$) rather than the axial direction (along $z$). The growth of the transverse boundary layer is arrested after a distance of order of the width, $W$, of the surface. Integrating Eq. (13) with $x$ as the independent variable from $x=0$ to $x=W$ for an average axial flow speed, $U$, and a transverse flow speed, $u_{\mathrm{trans}}$, the Sherwood number develops as stated in Eq. (14) for $z<z_{\mathrm{plat}}$, and in the following manner thereafter:

$$\mathrm{Sh}_{\mathrm{plat}} = \frac{(3/4)^{1/3}}{\Gamma\left(\frac{4}{3}\right)}\left(\frac{H}{W}\right)^{1/3}\left(\frac{H^2\dot{\gamma}_{\mathrm{trans}}}{D}\right)^{1/3}$$
$$= 0.81\left(\frac{H}{W}\right)^{1/3}\left(\frac{H\dot{\gamma}_{\mathrm{trans}}}{u_{\mathrm{trans}}}\right)^{1/3}\left(\frac{u_{\mathrm{trans}}}{U}\right)^{1/3}\mathrm{Pe}^{1/3}, \tag{15}$$

where the transverse shear rate, $\dot{\gamma}_{\mathrm{trans}}$, is defined by the transverse flow. We expect the entrance length, $z_{\mathrm{plat}}$, to scale inversely with the velocity ratio, $(u_{\mathrm{trans}}/U)$ due to the following simple argument: in the time that it takes for the transverse flow to traverse the width of the reactive surface, $t\sim W/u_{\mathrm{trans}}$ the axial flow has covered a distance

$$z_{\mathrm{plat}} = Ut \sim W\left(\frac{U}{u_{\mathrm{trans}}}\right). \tag{16}$$

As in the previous subsection, we would like to adapt these predictions [Eqs. (15) and (16)] for a reactive plate to the case of mass transfer from a 3D flow within a rectangular duct to a reactive wall. The prediction of the entrance length in Eq. (16) is unchanged. To evaluate the expression in Eq. (15), the dimensionless ratio $H\dot{\gamma}_{\mathrm{trans}}/u_{\mathrm{trans}}$ can be found by differentiating the transverse velocity with respect to $y$ at the reactive wall. We estimate the transverse shear rate at the reactive boundary as $\dot{\gamma}_{\mathrm{trans}}=u_{\mathrm{trans}}/H$. Plugging this estimate into Eq. (15), we arrive at the following prediction for the asymptotic value of the Sherwood number in 3D flows in ducts with a single reactive boundary:

$$\mathrm{Sh}_{\mathrm{plat}} = B_1\left(\frac{u_{\mathrm{trans}}}{U}\right)^{1/3}\mathrm{Pe}^{1/3} = B_1\mathrm{Pe}_{\mathrm{trans}}^{1/3}, \tag{17}$$

where $\mathrm{Pe}_{\mathrm{trans}}=u_{\mathrm{trans}}H/D$ is the transverse Péclet number, and $B_1$ is a geometry dependent constant that is $O(1)$ for the flows considered here for which $W=2H$.

Equations (14), (16), and (17) describe a modified version of the behavior observed in the solution to the Graetz problem: the evolution of Sh exhibits an entrance region in which Sh decreases as $z^{-1/3}$ and an asymptotic region in

which Sh takes on a constant value. Yet, the predicted Modified Graetz behavior has two important distinctions from the classic result:

(1) For a three-dimensional channel flow with a fixed ratio between the axial and transverse velocities (as in the case considered here), the entrance length, $z_{plat} \sim W(U/u_{trans})$ depends only on the ratio of the axial and transverse velocity components and not on the magnitude of $U$. Therefore $z_{plat}$ is a constant with respect to Pe; this behavior is distinct from the Graetz result for which $z_{plat} \sim \mathrm{PeH}$.
(2) The plateau value, $\mathrm{Sh}_{plat}$, in Eqs. (15) and (17) increases with Pe; this behavior is again distinct from the Graetz result for which $\mathrm{Sh}_{plat} = O(1)$.

The boundary layer picture presented here is simple, but, as we show in Sec. IV B, it captures many of the details of transfer to reactive boundaries in the presence of transverse flows. The assumption that the fluid impinging on the leading edge of the reactive surface is undepleted with respect to the bulk is not necessarily true for all transverse flows at all values of Pe. With a proper choice of flow, this assumption can be satisfied. Indeed, this assumption provides the key connection between mixing in the bulk and mass transfer to boundaries: the ability of a flow to homogenize the concentration boundary layer created by the transverse flow will determine the success or failure of that flow at maintaining a high constant value of Sh, and therefore also high rates of mass transfer. Thus, a transverse flow that provides efficient mixing in the bulk (e.g., a chaotic flow) should lead to larger, sustained rates of transfer than an equivalent (e.g., in magnitude) flow that does not mix well. This prediction is substantiated by our simulation results.

## IV. RESULTS AND DISCUSSION

### A. Qualitative results

We will discuss the results of our simulations qualitatively in this subsection and quantitatively in the next. Figure 4 demonstrates the growth of the concentration boundary layer for several flow geometries at $\mathrm{Pe} = 10^4$. The left column for each series is a gray scale plot of the concentration in the cross section, while the right column is a plot of the concentration averaged along the $x$ direction as a function of the $y$ coordinate.[30] The growth of the concentration boundary layer in the absence of a transverse flow is apparent and consistent with expectations. The boundary layer grows more quickly near the side walls due to the slower axial velocity and longer residence times in these regions. In the second half of the channel ($1000 \leqslant z/H \leqslant 2000$), the boundary layer fills the channel and the concentration distribution evolves in a self-similar manner.

With a transverse flow that produces one large vortex ($r=1$), the boundary layer at the ceiling evolves in two stages toward an asymptotic form: for short axial distances ($z/H \leqslant 80$), the depleted region remains thin due to the delivery of fresh solution to the "leading edge" of the ceiling (i.e., the top left corner) by the transverse flow; later, as the depleted solution encircles the entire cross section, the "feed stream" of the ceiling becomes depleted and the boundary layer grows to fill half the height of the channel. The recirculation of depleted solution back to the reactive boundary violates the assumption of homogenized concentration in our Lévêque treatment of the transverse boundary layer (Sec. III C); thus, we do not expect these flows to exhibit the modified Graetz behavior. Despite the eventual growth of the boundary layer to a thickness controlled by the geometry (i.e., $\sim H/2$), its initial, thin structure leads to a significantly larger drop in the average concentration than in a purely axial flow.

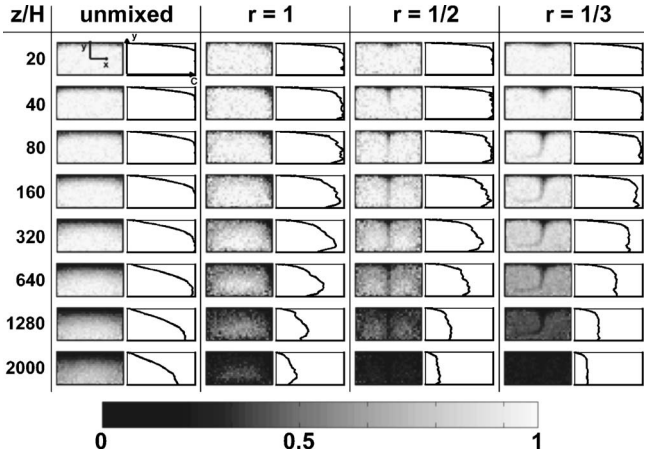


FIG. 4. Boundary layer development as a function of axial distance. The left frame for each column is the concentration profile in the cross section with concentration represented by gray scale values shown in the color bar at the bottom. The right frame is the concentration averaged along the $x$ direction as a function of $y$. In all cases, $\mathrm{Pe} = 10^4$ and the ratio of transverse velocity to axial velocity $u_{trans}/U = 0.2$. The leftmost column is a uniaxial flow. The middle two columns are nonchaotic, 3D flows as in Figs. 2(b) and 2(c). The rightmost column is a chaotic flow with $r = \frac{1}{3}$ and $L_{1/2} = 10H$ as in Fig. 2(a).

The results for flow with two constant vortices $\left(r = \frac{1}{2}\right)$ are similar to the single vortex case, but the boundary layer is entrained into the downwelling through the center of the channel rather than circling the walls. The complete recirculation of the depleted solvent back to the reactive boundary is again observed, but the effect is less pronounced than in the single vortex case. Due to this difference, the flow with $r = \frac{1}{2}$ is slightly more efficient than the flow with $r=1$ at decreasing average concentration.

Finally, the flow with $r = \frac{1}{3}$ has two asymmetric vortices that alternate sides of the channel periodically along the axial direction. The boundary layer that grows into the downwelling of this flow shifts back and forth with changes in the transverse flow; this movement is not apparent in the plots presented due to the fact that they were all taken at the end of cycles of the SHM at which point the concentration distributions have the same shape. Here the boundary layer transitions directly to a thin asymptotic structure. This behavior closely resembles the prediction of the Lévêque analysis presented in Sec. III C and was in fact our motivation for pursuing the concept of competing boundary layers. In this case, the depleted solution is injected into the large chaotic invariant set [see Fig. 2(a)] and homogenized such that solution with the average concentration is continuously delivered to the leading edge of the reactive boundary. Despite this dif-

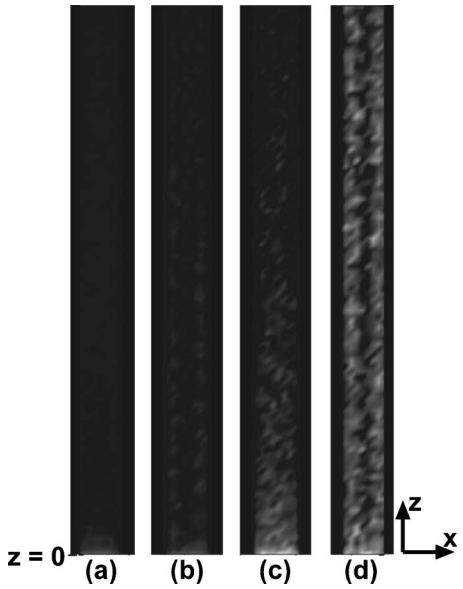


FIG. 5. Effect of transverse flow and Pe on flux profile along the ceiling of the channel. (a) Pe=$10^4$, no transverse flow. (b) Pe=$10^4$, with transverse flow. (c) Pe=$10^5$, no transverse flow. (d) Pe=$10^5$, with transverse flow. In (b) and (d): $r=1/3$, $L_{1/2}=10H$, ratio of transverse velocity to axial velocity $u_{\text{trans}}/U=0.2$. Note: the plots present a total channel length, $L_{\text{tot}}=200H$. The width of the channel has been magnified by a factor of 10 relative to the length for clarity.

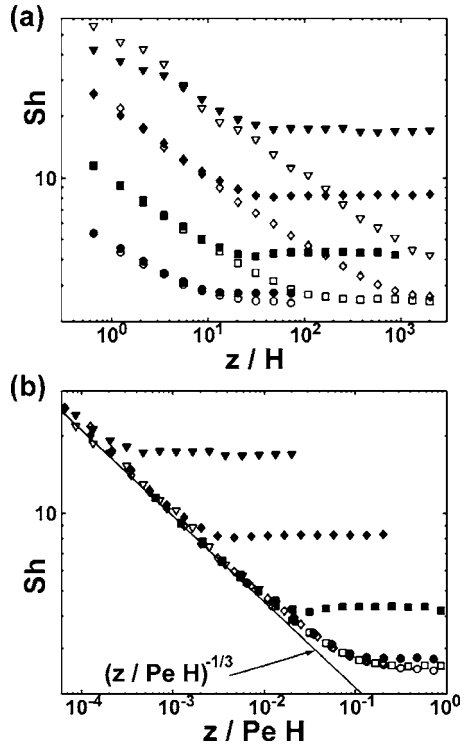


FIG. 6. Graetz and modified Graetz behavior. (a) Local Sherwood number Sh($z$) as a function of axial distance. (b) Sh($z$) as a function of axial distance scaled by Pe. Symbol shape indicates the value of Pe: circle—$10^2$, square—$10^3$, diamond—$10^4$, triangle—$10^5$. Open symbols are unstirred, filled symbols are chaotically stirred, $r=\frac{1}{3}$, $L_{1/2}=10H$, and $u_{\text{trans}}/U=0.2$. The straight line is the evolution of Sh($z$) as predicted in Eq. (14).

ference, the overall efficiency of this chaotic flow at transport toward the boundary is similar to that of the flow with $r=\frac{1}{2}$. This result suggests that while chaotic particle trajectories are vital to generating efficient mixing in the bulk, their effect on transfer to boundaries is more subtle. We will examine this question more thoroughly in Sec. IV B.

The qualitative effect of the transverse flow can also be seen in the profile of flux along the reactive surface.[30] Figure 5 shows the flux at the surface with and without transverse flow. The flux in the unstirred case drops quickly with axial distance. In the stirred case, the average flux is maintained at a higher, visible level for the entire length of the device. The pattern along the center of the flux profiles in the stirred cases is due to the migration of the downwelling between half-cycles.

## B. Quantitative results

### *1. Modified Graetz result with transverse flow*

We now turn our attention to a quantitative evaluation of interfacial mass transfer in the presence of transverse flows. In the standard solution to the Graetz-Nusselt problem, Sh($z$) is found to decrease as $z^{-1/3}$ in the entrance region, beyond which it takes on a constant value. Figure 6(a) shows Sh($z$) as a function of $z/H$ for the cases of pure uniaxial flow and chaotically stirred flow ($r=\frac{1}{3}$, $L_{1/2}=10H$). For all values of Pe($10^2-10^5$), both types of flow exhibit $z^{-1/3}$ scaling of Sh at the entry of the duct. The Sherwood number in the stirred cases diverges from the unstirred cases at $z/H\sim 20$, at which point it plateaus; we refer to this early transition to a constant asymptotic Sh as the modified Graetz behavior. This modified behavior is the benefit of transverse flows: Sh($z$) reaches its plateau earlier and at a higher value than without stirring. The plateau also appears at the same value of $z/H$ for each value of Pe, as predicted in Eq. (16) from our boundary layer picture (cf. Sec. III C). Figure 6(b) further shows that the unstirred cases exhibit a universal collapse when $z$ is scaled by Pe $H$, as expected from the standard Graetz solution.

In Fig. 7, the evolution of Sh in several flow geometries is compared to that for the strongly chaotic SHM flow ($r=1/3$, $L_{1/2}=10H$). As seen in Fig. 7(a), the mass transfer from the nonchaotic double vortex flow $\left(r=\frac{1}{2}\right)$ is similar to that from the chaotic flow in that Sh displays an entrance region of constant length followed by a (nearly) constant asymptotic value. We note though that Sh is slightly higher near the beginning of the plateau region and then decreases down the length of the channel rather than maintaining a constant value. The mass transfer from the single vortex flow ($r=1$) in Fig. 7(b) is again similar to that from the strongly chaotic flow, but Sh drops significantly at large $z/H$ and high Pe. This fall in the value of Sh is due to the depletion layer encircling the bulk and contaminating the feed stream as seen in Fig. 4 and discussed in Secs. III C and IV A. Figure 7(c) presents the mass transfer from a more weakly chaotic flow [$r=1/3$, $L_{1/2}=2.5H$; see Fig. 2(d)]; this flow clearly exhibits the modified Graetz behavior seen in the strongly chaotic flow despite the fact that the Poincaré maps of the two flows are substantially different (see Fig. 2).[27]

From the results in Fig. 7, it is apparent that the crucial ingredient for increasing transfer to boundaries is the presence of a strong transverse flow. Of secondary importance (at

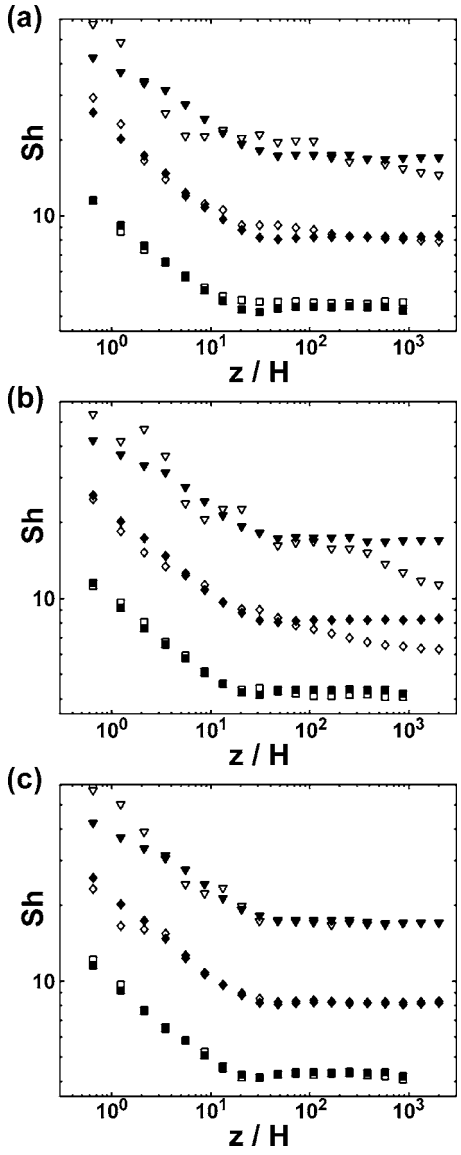


FIG. 7. Comparison of Sh($z$) for different flows. (a) Nonchaotic two vortex flow [$r=\frac{1}{2}$, as in Fig. 2(b)—open], chaotic two vortex flow [$r=1/3$, as in Fig. 2(a)—filled]. (b) Nonchaotic single vortex flow [$r=1$, as in Fig. 2(c)—open], chaotic two vortex flow [$r=\frac{1}{3}$, as in Fig. 2(a)—filled]. The nonchaotic flows are constant with respect to axial distance, while the chaotic flow shifts with a half cycle length $L_{1/2}=10H$. (c) Chaotic flows with $r=\frac{1}{3}$ showing the effect of a shorter half cycle. $L_{1/2}=2.5H$ [as in Fig. 2(d)—open], $L_{1/2}=10H$ [as in Fig. 2(a)—filled]. Symbol shape indicates the value of Pe: square—$10^3$, diamond—$10^4$, triangle—$10^5$. All flows have $u_{\text{trans}}/U=0.2$.

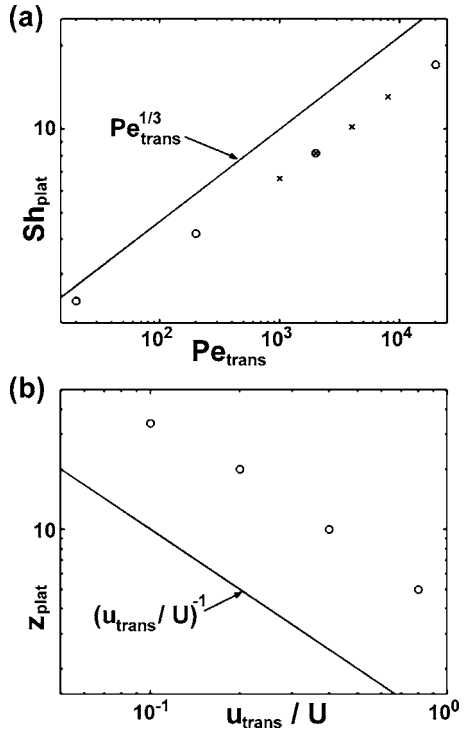


FIG. 8. Test of theoretical correlations against simulation. (a) $\text{Sh}_{\text{plat}}$ as a function of $\text{Pe}_{\text{trans}}=\text{Pe}(u_{\text{trans}}/U)$ in the presence of chaotic transverse flow: $r=\frac{1}{3}$, $L_{1/2}=10H$. Circles represent simulations with $u_{\text{trans}}/U=0.2$ at various values of Pe; crosses represent simulations with $\text{Pe}=10^4$ at various values of $u_{\text{trans}}/U$. The solid line shows the scaling predicted in Eq. (17). (b) Entrance length, $z_{\text{plat}}$ as a function of the ratio of floor slip velocity to average axial velocity in the presence of chaotic transverse flow: $r=\frac{1}{3}$, $L_{1/2}=10H$, $\text{Pe}=10^4$. These values of $z_{\text{plat}}$ were estimated from the elbows in plots of Sh($z$) such as those in Fig. 6. The solid line shows the scaling predicted in Eq. (16).

least in the regime explored here) is the complete homogenization of the transverse boundary layer before it returns to the reactive surface. The failure to meet this second condition appears in nonchaotic flows at large axial distance and high Pe.

### 2. Test of predicted scaling and correlations

In Fig. 8, we test the results of the Lévêque arguments presented in Sec. III C for the plateau values of the Sherwood number and the entrance length for the case of a strongly chaotic flow ($r=1/3$, $L_{1/2}=10H$). Figure 8(a) shows the scaling of $\text{Sh}_{\text{plat}}$ versus $\text{Pe}_{\text{trans}}=\text{Pe}(u_{\text{trans}}/U)$ taken from results such as those in Fig. 6 for various values of Pe and $(u_{\text{trans}}/U)$. This scaling relation from simulation is in good agreement with our theoretical prediction [Eq. (17)]. At the lowest value of Pe considered here ($\text{Pe}=100$, $\text{Pe}_{\text{trans}}=20$), $\text{Sh}_{\text{plat}}$ deviates from the expected scaling because the unstirred case, for which $\text{Sh}_{\text{plat}}=2.55$, gives a lower bound on the value of $\text{Sh}_{\text{plat}}$. Figure 8(b) presents the variation of the entrance length, $z_{\text{plat}}$, with $(u_{\text{trans}}/U)$ as measured approximately from results such as those in Fig. 6. The observed scaling $[z_{\text{plat}}\sim(u_{\text{trans}}/U)^{-1}]$ is as predicted in Eq. (16), with a prefactor somewhat larger than unity. We note again that Fig. 6 showed that, in unstirred cases, the entrance length is proportional to Pe $H$ while in stirred cases the entrance length is independent of Pe, as predicted by the standard and modified Graetz (Sec. III C) results. The following overall correlation for Sh($z$) is validated by Fig. 8:

$$\begin{aligned}\text{Sh}(z) &= B_0\left(\frac{\text{Pe}H}{z}\right)^{1/3} \qquad z < z_{\text{plat}},\\ \text{Sh}(z) &= B_1\left(\text{Pe}\frac{u_{\text{trans}}}{u_z}\right)^{1/3} \qquad z > z_{\text{plat}}\\ &= B_1\,\text{Pe}_{\text{trans}}^{1/3}\end{aligned} \tag{18}$$

with both $B_0$ and $B_1$ being $O(1)$. These results substantiate

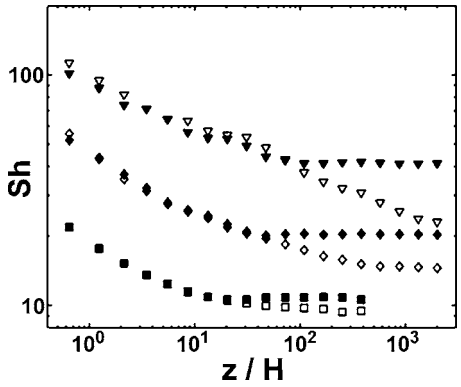


FIG. 9. Comparison of Sh for chaotic ($r=1/3$—filled) and nonchaotic ($r=\frac{1}{2}$—open) flows in the case of three reactive walls (e.g., ceiling and sidewalls). Symbol shape indicates the value of Pe: square—$10^3$, diamond—$10^4$, triangle—$10^5$. All flows have $u_{\text{trans}}/U=0.2$.

the simple boundary layer picture presented in Sec. III for this chaotic flow.

### 3. The role of Lagrangian chaos in mass transfer to no-slip boundaries

The similarity of the evolution of Sh shown in Fig. 7(a) for chaotic ($r=1/3$) and nonchaotic $\left(r=\frac{1}{2}\right)$ flows leads to the following question: What is the role of chaotic advection in mediating mass transfer to boundaries? The flows experienced by a particle near the reactive surface are quite similar in the two cases, with similar shear rates and initial structures of the depletion layers. The distinction appears in the path that the depleted fluid follows after it leaves the reactive boundary. In nonchaotic cases, the depleted fluid is stretched and reconcentrated by diffusive exchange with the bulk, but eventually returns to the reactive surface due to the unchanging transverse flow. This inevitable depletion of the feed stream of the reactive boundary results in a breakdown of the modified Graetz behavior as it allows the concentration profile to continue to evolve. This continued growth of the boundary layer precludes the establishment of a true plateau region until the boundary layer reaches the core of the vortices, and therefore fills the entire channel.

This behavior is contrasted by that in the chaotic flow ($r=1/3$) that is able to keep the depleted fluid from returning to the reactive surface for all Pe explored in this study ($10^2 \leqslant \text{Pe} \leqslant 10^5$, and $\text{Pe}=10^6$, data not shown). Figure 9 shows the difference in $\text{Sh}(z)$ for the flow with $r=1/3$ and the flow with $r=1/2$ where the ceiling and both sidewalls are taken to be reactive. The presence of more reactive surface area accentuates the difference between chaotic and nonchaotic flows, because it increases the challenge of mixing the depleted fluid before it returns to the reactive surface. We have also considered other flows ($r=5/12$, $r=1/3$ with various cycle lengths, ducts with square cross section); all of these flows show the modified Graetz behavior in the presence of chaos and continuously growing boundary layers in the absence of chaos.

The role of chaotic advection in defining the modified Graetz behavior can therefore be stated as the ability to ensure the delivery of undepleted fluid to the reactive surface independent of Pe and axial distance. In this sense, chaotic advection appears to be both necessary and sufficient for the existence of the modified Graetz behavior. It is necessary in the sense that nonchaotic flows fail to ensure this behavior, and sufficient in the sense that we have been unable to find a regime in which chaotic flows do not produce such behavior. We are currently developing more rigorous support of these conclusions.

### 4. Comparison to previous results

Our results share several similarities with those of other studies of heat and mass transfer in laminar flows. For the Dean flow in a helical tube, Janssen *et al.*, found Sh in the entrance region to scale with $\text{Pe}^{0.33}$ with additional dependence on Re; the Re dependence is likely due to the Re dependence of the transverse Dean flow.[20] They found however that the plateau value of Sh scales with $\text{Pe}^{1/6}$, while they noted that they expected scaling of $\text{Pe}^{1/3}$. Acharya *et al.*, found similar results for the enhancement to heat transfer in the same system.[22] They also extended the study to chaotic Dean flows by alternating the axis of the helical coil, and found an additional chaotic enhancement relative to nonchaotic flow that showed weak scaling in the Prandtl number Pr. Mokrani *et al.*, cited an enhancement of 13%–27% for heat transfer in chaotic over nonchaotic coiled tubes, although their results were presented in terms of enhancement to efficiency, and as specific values rather than in the form of a correlation; it is difficult to generalize their results and compare them to our own.[21] Khinast *et al.*, claim an enhancement in Sh that scales linearly with Re for mass transfer in a static mixer, although theoretical justification of this scaling is not presented.[1] A system that has been studied in more depth is that of heat or mass transfer to the surface of particles in packed beds. Our results bear a similarity to established correlations for packed beds, for which the local Sherwood number scales as $\text{Pe}^{1/3}$.[13] The velocity ratio ($u_{\text{trans}}/U$) for a packed bed is typically fixed, thus it does not appear explicitly in the correlations as it does in our Eq. (17). Our boundary layer treatment appears to provide a valid explanation of transfer from 3D laminar flows and may lead to a deeper understanding of transfer to boundaries in other laminar reactors.

### 5. Design considerations

To provide insight into the use of this information for design purposes, we consider here the design of a microreactor. For given cross-sectional dimensions ($H,W$), transverse flow ($u_{\text{trans}}/U$), and diffusivity of reactants, the design of a reactor requires the choice of the total length of the channel, $L_{\text{tot}}$, and the flow speed (or Pe). The parameters that we use to define the performance of the system are the overall efficiency, $\varepsilon$, and the total current delivered to the surface, $\dot{N}$ (mol/s). The efficiency is defined as the fractional number of particles that have reacted before the outlet of the channel:

$$\varepsilon = \frac{\dot{N}_{\text{in}} - \dot{N}_{\text{out}}}{\dot{N}_{\text{in}}} = \frac{C_{\text{cup}}(0) - C_{\text{cup}}(L_{\text{tot}})}{C_{\text{cup}}(0)} = 1 - \frac{C_{\text{cup}}(L_{\text{tot}})}{C_{\text{cup}}(0)}, \tag{19}$$

where $\dot{N}_{\text{in}}$ (mol/s) and $\dot{N}_{\text{out}}$ (mol/s) are the molar flow rate of reactant in and out of the device, respectively, and $L_{\text{tot}}$ (m) is the total length of the device. The total current is then

$$\dot{N} = (C_{\text{cup}}(0) - C_{\text{cup}}(L_{\text{tot}}))Q = C_{\text{cup}}(0)\varepsilon HWU = C_{\text{cup}}(0)\varepsilon DW\text{Pe}, \tag{20}$$

where $Q$ ($m^3/s$) is the volumetric flow rate of solution, $D$ ($m^2/s$) is the diffusivity of the solute, and $H$ (m) and $W$ (m) are the height and width of the channel, respectively. Equation (20) indicates that for a given width of channel and concentration and diffusivity of the reactive solute, specification of $\varepsilon$ and $\dot{N}$ uniquely specifies the Pe at which the system must operate. The expression for efficiency in Eq. (19) can then be used to specify the length of device for a given form of $C_{\text{cup}}(L_{\text{tot}})$. Although $C_{\text{cup}}(L_{\text{tot}})$ is generally a complicated function, we can find a simple approximate expression for the common scenario of high efficiency. For high efficiencies ($\varepsilon > 0.5$), the required length is long compared to the length of the entrance region ($L_{\text{tot}} > 4z_{\text{plat}}$). Integrating Eq. (6) from the inlet up to length $L_{\text{tot}} > z_{\text{plat}}$, the average concentration evolves according to

$$\frac{C_{\text{cup}}(L_{\text{tot}})}{C_{\text{cup}}(0)} = \frac{C_{\text{cup}}(z_{\text{plat}})}{C_{\text{cup}}(0)}\frac{C_{\text{cup}}(L_{\text{tot}})}{C_{\text{cup}}(z_{\text{plat}})} = \exp\left(-\frac{3}{2}\left(\frac{z_{\text{plat}}}{\text{Pe}\,H}\right)^{2/3}\right)\exp\left(-\frac{Sh_{\text{plat}}}{\text{Pe}}\frac{L_{\text{tot}} - z_{\text{plat}}}{H}\right) \sim \exp\left(-\frac{\text{Sh}_{\text{plat}}}{\text{Pe}}\frac{L_{\text{tot}}}{H}\right). \tag{21}$$

This last expression implies the approximation, $\text{Sh}(z) \sim \text{Sh}_{\text{plat}}$ throughout the length of the reactor. Although $\text{Sh}(z)$ is strictly larger than $\text{Sh}_{\text{plat}}$ in the entrance region, this approximation is true to within several percent for all flows (uniaxial and 3D) considered in this work. As a further illustration of the appropriateness of the approximate expression for $C_{\text{cup}}(L_{\text{tot}})$ in Eq. (21), the semilog plots in Fig. 10 show that the evolution of $C_{\text{cup}}(L_{\text{tot}})$ from simulations are nearly linear with slope $\text{Sh}_{\text{plat}}/\text{Pe}$. Therefore, using Eqs. (21) and (19), we express the efficiency as

$$\varepsilon = 1 - \frac{C_{\text{cup}}(L_{\text{tot}})}{C_{\text{cup}}(0)} = 1 - \exp\left(-\frac{Sh_{\text{plat}}}{\text{Pe}}\frac{L_{\text{tot}}}{H}\right). \tag{22}$$

Equation (22) gives an expression for the length of the device in terms of the specified efficiency and Pe, as determined above:

$$\frac{L_{\text{tot}}}{H} \sim -\frac{\ln(1-\varepsilon)\text{Pe}}{\text{Sh}_{\text{plat}}}. \tag{23}$$

In the case of the SHM flow ($r = 1/3$, $L_{1/2} = 10H$, $u_{\text{trans}}/U = 0.2$) for which Eq. (18) provides a correlation for $\text{Sh}_{\text{plat}}$, we can rewrite Eq. (23) as

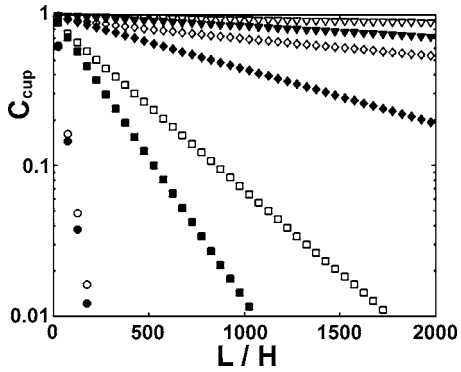


FIG. 10. Cup mixing concentration as a function of total device length, $L_{\text{tot}}$. Symbol shape defines Pe: circle—$10^2$, square—$10^3$, diamond—$10^4$, triangle—$10^5$. Open symbols are unstirred, filled symbols are with chaotic transverse flow: $r = \frac{1}{3}$, $L_{1/2} = 10H$, $u_{\text{trans}}/U = 0.2$.

$$\frac{L_{\text{tot}}}{H} \sim -\frac{\ln(1-\varepsilon)\text{Pe}^{2/3}}{B_1\left(\frac{u_{\text{trans}}}{U}\right)^{1/3}}. \tag{24}$$

Thus, in summary, one can use $\varepsilon$ and $\dot{N}$ in Eq. (20) to determine the required Pe, and $\varepsilon$ and Pe in Eq. (23) to determine $L_{\text{tot}}$. We note that for a given efficiency, the ratio of the length of device required for pure axial flow to the length required in the presence of the SHM chaotic flow is

$$\frac{L_{\text{tot}}^{\text{unstirred}}}{L_{\text{tot}}^{\text{stirred}}} \sim \frac{\text{Sh}_{\text{plat}}^{\text{stirred}}}{\text{Sh}_{\text{plat}}^{\text{unstirred}}} \sim \frac{B_1\left(\frac{u_{\text{trans}}}{U}\right)^{1/3}\text{Pe}^{1/3}}{2.55}, \tag{25}$$

where $\text{Sh}_{\text{plat}}^{\text{unstirred}} \approx 2.55$ is approximated from the plot in Fig. 6(b). If we take $B_1 \sim 0.75$ [inferred from Fig. 8(a)], the unstirred device must be nearly twice the length of the stirred device at $\text{Pe} = 10^3$ and more than eight times the length of the stirred device at $\text{Pe} = 10^5$ for a flow with $u_{\text{trans}}/U = 0.2$. The scaling predicted in Eq. (25) holds for any duct flow (with $L_{\text{tot}} \gg z_{\text{plat}}$) that provides the modified Graetz behavior. As a further illustration of increased transfer due to transverse flow, Fig. 11 shows the efficiency and total current from the simulation results for a device of length 2000 $H$, where $H$ is the height of the channel. At $\text{Pe} = 10^5$, the efficiency and total current are ~3 fold higher with the SHM flow than without it. Figure 11 also illustrates that the difference between chaotic and nonchaotic flows only becomes appreciable at high Pe.

## V. CONCLUSIONS

In conclusion, our simulations indicate that 3D laminar flows of all types lead to increased rates of mass transfer to reactive boundaries in microchannels relative to uniaxial flows. We developed a treatment for the evolution of the concentration distribution from Lévêque-type arguments, and we validated predictions from this simple treatment with simulation results. By comparing several flows, we identified the characteristics of a flow that are important for increasing mass transfer to boundaries: (1) a high transverse shear rate at the reactive boundary; this property is of primary impor-

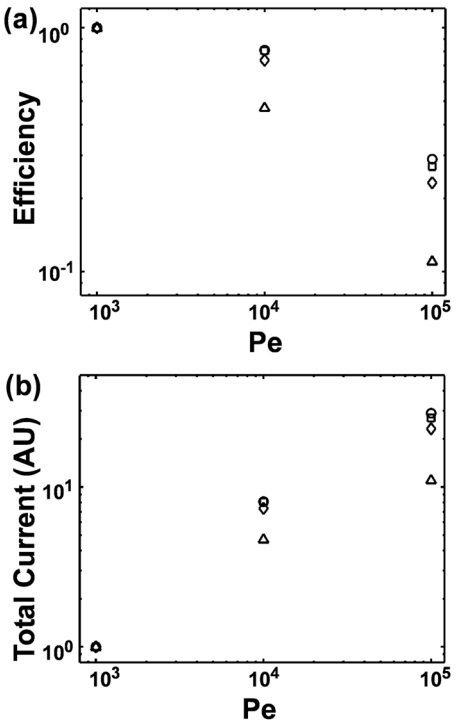


FIG. 11. Efficiency and total current from simulation results for a device of length $L_{tot}=2000H$. Triangles represent uniaxial flow, diamonds represent stirred flows with $r=1$, squares represent $r=1/2$, and circles represent $r=1/3$ with $L_{1/2}=10H$ and $u_{trans}/U=0.2$. Efficiency and total current are defined in Eqs. (19) and (20), respectively.

tance to increase the average rates of transfer relative to those from uniaxial flows. (2) The ability to homogenize the concentration boundary layer before it returns to the reactive boundary; this characteristic leads to a modified Graetz behavior. This behavior is attractive due to the simplicity of the analysis it allows, as illustrated in Sec. IV B 5. The existence of this second property appears to distinguish chaotic 3D flows from nonchaotic ones: chaotic advection appears to be both necessary and sufficient to ensure the complete homogenization of the depleted solution before returning it to the reactive surface.

We note that the position of the reactive boundary that we have considered is not optimal with respect to benefiting from the transverse flows generated by a grooved boundary. Nonetheless, this geometry is experimentally convenient, as a microchannel that contains the appropriate groove structure can simply be sealed to a reactive surface. Furthermore, rates of transfer are substantially increased in this geometry at high Pe. We expect more significant increases in transfer rates for reactions on the grooved surface itself, as the transverse flows are strongest in this region. Simulation of such systems will require a full computational fluid dynamics description of the flow in the vicinity of the grooves, and we have left this study for later investigation. We are pursuing experimental validation of these results and further theoretical clarification of the role of chaotic advection in defining the modified Graetz behavior.

## ACKNOWLEDGMENTS

The authors wish to thank Eric Siggia and Donald Koch for helpful conversations. This work was funded by a Start-Up Grant from the North American Mixing Forum, the National Science Foundation (CTS-0529042), and the Department of Energy (DE-FG02-05ER46250).

[1] J. G. Khinast, A. Bauer, D. Bolz, and A. Panarello, "Mass-transfer enhancement by static mixers in a wall-coated catalytic reactor," Chem. Eng. Sci. **58**, 3 (2003).
[2] R. Ferrigno, A. D. Stroock, T. D. Clark, M. Mayer, and G. M. Whitesides, "Membraneless vanadium redox fuel cell using laminar flow," J. Am. Chem. Soc. **124**, 44 (2002).
[3] E. R. Choban, L. J. Markoski, A. Wieckowski, and P. J. A. Kenis, "Microfluidic fuel cell based on laminar flow," J. Power Sources **128**, 1 (2004).
[4] J. L. Cohen, D. A. Westly, A. Pechenik, and H. D. Abruna, "Fabrication and preliminary testing of a planar membraneless microchannel fuel cell," J. Power Sources **139**, 1 (2005).
[5] M. L. Yarmush, D. B. Patankar, and D. M. Yarmush, "An analysis of transport resistances in the operation of BIAcore(TM): Implications for kinetic studies of biospecific interactions," Mol. Immunol. **33**, 15 (1996).
[6] D. G. Myszka, T. A. Morton, M. L. Doyle, and I. M. Chaiken, "Kinetic analysis of a protein antigen-antibody interaction limited by mass transport on an optical biosensor," Biophys. Chem. **64**, 1 (1997).
[7] V. Sikavitsas, J. M. Nitsche, and T. J. Mountziaris, "Transport and kinetic processes underlying biomolecular interactions in the BIACORE optical biosensor," Biotechnol. Prog. **18**, 4 (2002).
[8] H. C. Chang and M. Sen, "Application of chaotic advection to heat transfer," Chaos, Solitons Fractals **4**, 6 (1994).
[9] S. C. Jana and J. M. Ottino, "Chaos-enhanced transport in cellular flows," Philos. Trans. R. Soc. London, Ser. A **338**, 1651 (1992).
[10] A. D. Stroock, S. K. W. Dertinger, A. Ajdari, I. Mezic, H. A. Stone, and G. M. Whitesides, "Chaotic mixer for microchannels," Science **295**, 5555 (2002).
[11] A. D. Stroock, S. K. Dertinger, G. M. Whitesides, and A. Ajdari, "Patterning flows using grooved surfaces," Anal. Chem. **74**, 20 (2002).
[12] A. D. Stroock and G. J. McGraw, "Investigation of the staggered herringbone mixer with a simple analytical model," Philos. Trans. R. Soc. London, Ser. A **362**, 1818 (2004).
[13] R. B. Bird, W. E. Stewart, and E. N. Lightfoot, *Transport Phenomena*, 2nd ed. (Wiley, Danvers, 2002).
[14] T. Nishimura and K. Kunitsugu, "Fluid mixing and mass transfer in two-dimensional cavities with time-periodic lid velocity," Int. J. Heat Fluid Flow **18**, 5 (1997).
[15] V. Ganesan, M. D. Bryden, and H. Brenner, "Chaotic heat transfer enhancement in rotating eccentric annular-flow systems," Phys. Fluids **9**, 5 (1997).
[16] S. Ghosh, H. C. Chang, and M. Sen, "Heat-transfer enhancement due to slender recirculation and chaotic transport between counter-rotating eccentric cylinders," J. Fluid Mech. **238**, 119 (1992).
[17] E. Saatdjian, N. Midoux, M. I. G. Chassaing, J. C. Leprevost, and J. C. Andre, "Chaotic mixing and heat transfer between confocal ellipses: Experimental and numerical results," Phys. Fluids **8**, 3 (1996).
[18] J. C. Leprevost, A. Lefevre, J. P. Brancher, and E. Saatdjian, "Chaotic mixing and heat transfer in a periodic 2D flow," C. R. Acad. Sci., Ser. IIb: Mec., Phys., Chim., Astron. **325**, 9 (1997).
[19] E. Saatdjian and J. C. Leprevost, "Chaotic heat transfer in a periodic two-dimensional flow," Phys. Fluids **10**, 8 (1998).
[20] L. A. M. Janssen and C. J. Hoogendoorn, "Laminar convective heat-transfer in helical coiled tubes," Int. J. Heat Mass Transfer **21**, 9 (1978).
[21] A. Mokrani, C. Castelain, and H. Peerhossaini, "The effects of chaotic advection on heat transfer," Int. J. Heat Mass Transfer **40**, 13 (1997).
[22] N. Acharya, M. Sen, and H. C. Chang, "Analysis of heat transfer enhancement in coiled-tube heat exchangers," Int. J. Heat Mass Transfer **44**, 17 (2001).
[23] T. Lemenand and H. Peerhossaini, "A thermal model for prediction of the Nusselt number in a pipe with chaotic flow," Appl. Therm. Eng. **22**, 15 (2002).
[24] J. M. Ottino, *The Kinematics of Mixing: Stretching, Chaos, and Transport* (Cambridge University Press, Cambridge, 1989).
[25] W. H. Press, S. A. Teukolsky, W. T. Vetterling, and B. P. Flannery, *Nu-*

*merical Recipes in C: the Art of Scientific Computing*, 2nd ed. (Cambridge University Press, New York, 2002).
[26]D. A. McQuarrie, *Statistical Mechanics* (Harper, New York, 1976).
[27]In the case of $L_{1/2}=2.5H$, our approximate representation of the transition from one form of transverse flow to another as instantaneous [see Fig. 1(b)] may result in an overestimate of the transverse displacement per half-cycle. Nonetheless, this case is representative of physically realizable flows with small transverse displacements and distinct structure in their Poincaré maps [see Fig. 2(d)].
[28]Efficiency $\varepsilon(z)$, current density, and sensor response time are related to $\mathrm{Sh}(z)$ as follows: $\varepsilon(z)=$amount reacted/amount introduced$=1-\exp(-\int \mathrm{Sh}(z')dz'/\mathrm{Pe}H)$ where the limits of the integral are from $z'=0$ to $z'=z$; current density is proportional to total current, which is proportional to Pe $\varepsilon(z)$; sensor response time is inversely proportional to total current. Therefore by maximizing $\mathrm{Sh}(z)$, one can increase efficiency and current density and decrease sensor response time.
[29]J. L. Xu, Y. H. Gan, D. C. Zhang, and X. H. Li, "Microscale heat transfer enhancement using thermal boundary layer redeveloping concept," Int. J. Heat Mass Transfer **48**, 9 (2005).
[30]The noise in these plots is due to the finite size of the population of tracers that we employed. We did not run more particles to eliminate this noise because these concentration distributions are only meant to convey qualitative information. The number of tracers was sufficient to ensure convergence of the locally averaged values of concentration used in evaluating mass transfer coefficients.